

Detection and elimination of signal errors due to unintentional movements in biomedical magnetic induction tomography spectroscopy (MITS)

S. Issa^{1,2} and H. Scharfetter¹

1. Institute of Medical Engineering, Graz University of Technology, Graz, Austria
2. E-mail any correspondence to: sinan@sbox.tugraz.at

Abstract

In biomedical MITS, slight unintentional movements of the patient during measurement can contaminate the aimed images to a great extent. This study deals with measurement optimization in biomedical MITS through the detection of these unpredictable movements during measurement and the elimination of the resulting movement artefacts in the images to be reconstructed after measurement. The proposed detection and elimination (D&E) methodology requires marking the surface of the object under investigation with specific electromagnetically perturbing markers during multi-frame measurements. In addition to the active marker concept already published, a new much simpler passive marker concept is presented. Besides the biological signal caused by the object, the markers will perturb the primary magnetic field inducing their own signals. The markers' signals will be used for the detection of any unwanted object movements and the signal frames corrupted thereby. The corrupted signal frames will be then excluded from image reconstruction in order to prevent any movement artefacts from being imaged with the object. In order to assess the feasibility of the developed D&E technique, different experiments followed by image reconstruction and quantitative analysis were performed. Hereof, target movements were provoked during multifrequency, multiframe measurements in the β -dispersion frequency range on a saline phantom of physiological conductivity. The phantom was marked during measurement with either a small single-turn coil, an active marker, or a small soft-ferrite plate, a passive marker. After measurement, the erroneous phantom signals were corrected according to the suggested D&E strategy, and images of the phantom before and after correction were reconstructed. The corrected signals and images were then compared to the erroneous ones on the one hand, and to other true ones gained from reference measurements wherein no target movements

were provoked on the other hand. The obtained qualitative and quantitative measurement and image reconstruction results showed that the erroneous phantom signals could be accurately corrected, and the movement artefacts could be totally eliminated, verifying the applicability of the novel D&E technique in measurement optimization in biomedical MITS and supporting the proposed aspects.

Keywords: Magnetic induction tomography spectroscopy; movement errors; imaging; movement artefacts; active marker; passive marker; detection and elimination.

Introduction

Magnetic induction tomography spectroscopy (MITS), the combination of magnetic induction tomography (MIT) [1, 2, 3] and magnetic induction spectroscopy (MIS) [4, 5], is a contactless, non-invasive near-field imaging modality aiming at the reconstruction of the passive electromagnetic properties (PEP) of different materials. MITS requires time-harmonic excitation (primary) magnetic fields to be coupled from a transmitting coil array to the material under investigation. As a direct consequence, eddy currents will be induced in the investigated material perturbing the excitation fields and inducing in turn perturbation (secondary) magnetic fields. The perturbation fields are then measured in form of voltages by means of a receiving coil array. These voltages represent the useful MITS signals, which carry the desired information about the PEP distributions in the investigated material.

In biomedical MITS, the unintentional movements of the patient during measurement can sometimes cause an undesired signal change as large as the useful signal itself or even larger. If these unwanted movements can be detected during measurement, and the resulting signal errors can be cancelled out prior to image reconstruction, then some kind of filter is established to get rid of the resulting movement artefacts in the images to be reconstructed.

Heretofore, studies in this regard have rarely been published. In [6, 7], the authors suggested tracking the investigated object through mounting switchable small single-turn coils on its surface and reconstructing their positions. The gained tracking information, i.e., the reconstructed positions of the coils, might then be used in a proper way to correct the movement artefacts. While [6] called such coils *active reference signal generators* due to the proposed function and mode of operation, [7], for the same reason, called them *active markers* and suggested using a MOSFET as a switch for each coil marker. When the MOSFET is *switched on*, the marker coil is shorted and additional eddy currents will be induced; hence, both the object and marker signals will be available whereby the object and the marker's position could be reconstructed, respectively. When the MOSFET is *switched off* and thereby the marker loop is opened, there will be no additional induction of eddy currents; hence, there will be no signal available except that caused by the object, and the marker would be invisible in the reconstructed object image. Thus, on the one hand, the tracking idea of [6, 7] requires the reconstruction of the exact positions of the markers on the object surface which might be achieved by means of an appropriate iterative reconstruction algorithm for the nonlinear MITS problem; on the other hand, it requires another appropriate algorithm to eliminate the movement artefacts in the object images based on the reconstructed markers' positions.

While these ideas are attractive, there are two caveats:

1. The required image reconstruction and correction algorithms are computationally very expensive.
2. The active markers require additional electronic control circuitry and the synchronization of this circuitry with the imaging device. In addition, parasitic eddy currents may be induced in the metallic parts contained in this circuitry, which might contaminate the useful MITS signal.

Concerning (1), in this study, a novel technique will be presented for the detection of unintentional target movements during measurement and the elimination of the resulting motion artefacts in the images to be reconstructed after measurement. This technique will be termed *detection and elimination* and abbreviated as *D&E*. The D&E concept is much simpler and hence easier to

implement because it neither requires the time-consuming reconstruction of the markers on the target surface nor the complex analysis and correction of the target motion during measurement for artefact elimination.

Concerning (2), we present a new so-called *passive marker* concept as an alternative for the MOSFET-switched *active marker* described in [7], which was also used in this study. This development was motivated by the need for a simple movement detection sensor without complex implementation or a complicated measurement protocol. In contrast to the active marker, the new passive marker requires no electric or electronic parts at all for its operation because it is *permanent*, i.e., it requires *no on-off switching* during measurement to accomplish the error detection function. Consequently, on the one hand, the MITS measurement retains its advantageous contactless measurement manner; on the other hand, the associated measurements take half of the time in comparison to those with the active (coil) marker which requires two separate acquisitions during the *on* and *off* phases, respectively. Moreover, the implementation of the passive marker concept is amazingly cheap.

The applicability of the novel D&E technique in measurement optimization in biomedical MITS using an active and a passive marker was assessed. For this purpose, multifrequency, multiframe measurements were conducted in the low part of the β -dispersion frequency range with a marker mounted on the lateral surface of a conducting background medium containing a test phantom, both of physiological conductivity. The target medium was slightly moved during measurement in order to simulate an unintentional movement. The resulting real measurement data were analysed and processed according to the proposed D&E methodology, and images of the conductivity distribution within the target medium were subsequently reconstructed.

Materials and methods

D&E technique

1. *D&E principle*

The main principle underlying the D&E methodology is based on *weak primary field perturbations* caused by biological materials described in [4, 5, 8, 9]. In this case, the biomedical MITS signal is dominated by its imaginary part corresponding to the conductivity contribution, whereas its real part essentially contains the permittivity and permeability (susceptibility) contributions which can usually be neglected in the low part of the β -dispersion frequency range. In line therewith, the complex conductivity $\{y = \sigma + j\omega\epsilon_0\epsilon_r\}$ (σ , j , ω , ϵ_0 and ϵ_r are the electrical conductivity, imaginary unit, angular frequency, vacuum and relative permittivity, respectively) can be reduced -in good approximation- to its real part, the conductivity term, i.e., $\{y \approx \sigma\}$. In contrast to biological materials, high-conductive

or magnetically high-permeable materials induce *strong primary field perturbations* and thereby strong quasi-pure real signals reflecting conductivity and permeability contributions, respectively.

Based on the aforementioned assumptions, if specifically chosen materials or objects that *strongly perturb the primary field* are employed as markers on the surface of the target medium, the *target* and *marker* will induce *imaginary* and *real* signals, respectively. Thus, if the *marked target* (a target with one or more markers mounted on its surface) unintentionally undergoes any kind of motion during measurement, then the *target signal* and *marker signal* will change accordingly. The change in the latter (real) one represents the *detection signal* to be used to identify the motion, whilst the change in the former (imaginary) one represents the motion-induced *signal error* to be eliminated. This procedure is illustrated in figure (1).

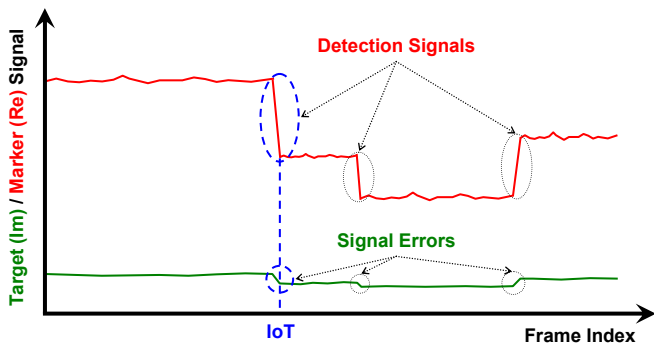


Fig. 1: Functional mechanism of the D&E technique. Green curve: imaginary target signal, red curve: real marker signal; IoT: index of truncation. The sharp jumps in the marker signal indicate the occurrence of unwanted target movements during measurement, and help to detect the corresponding erroneous changes in the target signal, which are of too small magnitudes.

The D&E method assumes that the MITS measurements are to be carried out in a multiframe manner. If unintentional target movements occur during measurement, they will cause remarkable changes in the marker signal. These changes represent *detection signals* where the one corresponding to the first movement pinpoints the *index of truncation (IoT)* required for the D&E process. Thus, the IoT is the index of that frame at which the very first unwanted movement occurs. Consequently, all target frames with index $\{i \geq IoT\}$ are affected by movement errors and have to be removed, whereas all remaining frames with index $\{i < IoT\}$ are free of movement errors and can thus be used for image reconstruction.

The quality of the images corrected by the D&E method depends only on the quality of the remaining error-free frames after the error elimination procedure of the D&E process, namely, $\{i < IoT\}$, i.e., on their reliability regarding noise, drifts, outliers, etc. Thus, even if an unwanted movement occurs immediately after the first acquired frame, i.e., if $IoT = 2$, then the one single remaining frame

will deliver a useful image if it is reliable. If it comes to the worst and an unwanted movement occurs at the very first frame, i.e., if $IoT = 1$, then the D&E process reduces to its error detection procedure informing that $IoT = 1$ and signifying therewith that the performed measurement failed and needs to be repeated.

The introduction of the IoT represents a quick and simple form of error detection but can also give rise to misclassifications. It is of importance not to reject data of interest that also causes fluctuations in the real part due to physiologic signals, such as the periodic change caused by breathing and cardiac activity. In such cases more sophisticated methods may be required, e.g., by assessing the signal dynamics in comparison with a priori known patterns from physiological signals, e.g., by matched filters. A first simple approach could be the identification of a certain threshold for the magnitude of the jump in the real part corresponding to the IoT. The a priori information can be gained from reference measurements wherein a sufficient set of the intended markers are distributed on the patient's surface. In any case, the threshold should be large enough so as to prevent misclassifications due to noise. An appropriate criterion in this respect may be to define or accept a *first marker signal change* as the *detection signal* with the IoT if this change is at least two orders of magnitude higher than the noise level (standard deviation) of the marker signal.

2. D&E with active markers (active D&E)

In active D&E, the marker mounted on the target surface can be *switched on and off* during measurement, which can be exemplified by the active (coil) marker of [6, 7]. If any unintentional movements occur, then during the *on* phase, these movements lead to the distortion of the target (imaginary) signal and to the induction of the detection (real) signal by the marker, whereas during the *off* phase, no signal except the distorted one of the target will be induced. Thus, the real frame whereat the marker signal shows the first sharp change marks the IoT.

As regards the target signal to be cleared of movement errors, it can be chosen between the two ones received during the *on* and *off* phases of the marker, respectively, based on some criterion, e.g., noise, outliers, etc. Better would be however to correct both of them and then to chose.

3. D&E with passive markers (passive D&E)

In passive D&E, the marker mounted on the target surface has a *permanent* effect during measurement due to the material whereof it is made, e.g., a ferromagnetic material, which induces *strong primary field perturbations*. Thus, in contrast to the active marker, the passive marker yields a *permanent* signal. An active (coil) marker induces the *strong primary field perturbations* due the eddy currents induced

in the coil only when the coil is *switched on*, i.e., its signal is *non-permanent*. Anyway, again, the real frame whereat the passive marker signal shows the first sharp jump identifies the IoT.

The ferromagnetic material must have a low loss factor because otherwise it does not produce a purely real signal. Hence, the imaginary part μ_r'' of its relative magnetic permeability $\{\mu_r = \mu_r' - j * \mu_r''\}$ must be much lower than the real one μ_r' . Otherwise, μ_r'' causes spurious imaginary signals, which are then confused with the target signal.

4. Measurement model

Figure (2) illustrates a simplified equivalent measurement diagram illustrating a *marked biological target* located in the space between the transmitter and the receiver. In the real electric implementation of the coil system, all coils were electrostatically well shielded so that no parasitic capacitive coupling greater than the measurement noise level could be registered. Therefore, figure (2) and the associated analysis only consider the inductive coupling between the different components. Additionally, due to the very small dimensions of the used marker in comparison to the target medium in the real measurement setup (15.55 ℓ saline tank containing a test phantom, see figure 5), the mutual coupling between the target medium and the marker is considered to be insignificant in the following analysis and is not considered in figure (2).

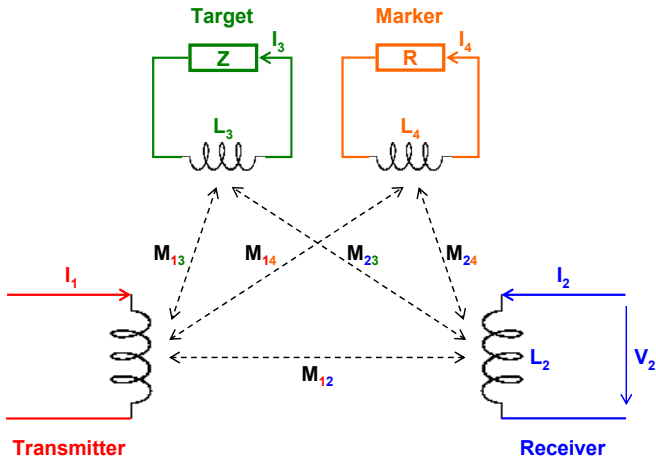


Fig. 2: Equivalent measurement model for a *marked biological target* in biomedical MITS. Z and R represent the impedance and resistance of the target and marker, respectively; $L_{\#}$, $I_{\#}$ and $V_{\#}$ represent the inductance, current and voltage, respectively, with respect to the indexed component; $M_{\#\#}$ represents the mutual inductance between the two indexed components.

Based on the inductive coupling model in figure (2), and taking into consideration the high-impedance termination of the receiving coil in the actual measurement system, i.e., $I_2 = 0$, the received signal at L_2 reads as follows:

$$V_2 = I_1 \cdot j\omega M_{12} + I_3 \cdot j\omega M_{23} + I_4 \cdot j\omega M_{24} \quad (1)$$

I_3 and I_4 can be explicitly stated with respect to I_1 through reformulation of the following transmitter-target and transmitter-marker relationships (2, 3), respectively:

$$I_1 \cdot j\omega M_{13} + I_3 (Z + j\omega L_3) = 0 \quad (2)$$

$$I_1 \cdot j\omega M_{14} + I_4 (R + j\omega L_4) = 0 \quad (3)$$

which results in the following equations, respectively:

$$I_3 = -I_1 \frac{j\omega M_{13}}{Z + j\omega L_3} \quad (4)$$

$$I_4 = -I_1 \frac{j\omega M_{14}}{R + j\omega L_4} \quad (5)$$

Thus, inserting equations (4, 5) in equation (1), the received signal at L_2 reads then finally as follows:

$$V_2 = I_1 \cdot j\omega M_{12} + I_1 \omega^2 \frac{M_{13} M_{23}}{Z + j\omega L_3} + I_1 \omega^2 \frac{M_{14} M_{24}}{R + j\omega L_4} \quad (6)$$

where the first right-hand-side term corresponds to the primary field and represents the carrier signal to be suppressed as much as possible, whilst the second and third ones correspond to the secondary field and represent the useful target and marker signals, respectively.

Equation (6) can be rewritten in an approximated version after making some assumptions. Thus, if $\{|Z| \gg \omega L_3\}$ and the resistive term R_T of the target impedance $\{Z = R_T + 1/j\omega C_T\}$ dominates over its capacitive term $1/j\omega C_T$, (R_T and C_T are not shown in figure 2), i.e., if $\{Z \approx R_T\}$, and if the marker is carefully chosen so that $\{R \ll \omega L_4\}$, then a simplified version of equation (6) can be stated as follows:

$$V_2 = I_1 \cdot j\omega M_{12} + I_1 \omega^2 \frac{M_{13} M_{23}}{R_T} + I_1 \omega^2 \frac{M_{14} M_{24}}{j\omega L_4} \quad (7)$$

When defining the excitation current I_1 as the reference signal (*phase* = 0°), then the second and third right-hand-side terms represent now a pure *imaginary target signal* and a pure *real marker signal*, respectively.

The two factors $M_{13} M_{23}$ and $M_{14} M_{24}$ depend on the position of the target and the marker, respectively, with respect to the transmitter and receiver. As can be seen in equation (8), these two factors represent the key quantities when observing a change in the received signal due to a change in the position of the *marked target* caused by some movement:

$$\frac{\partial V_2}{\partial (x, y, z)} = I_1 \omega^2 \frac{\partial (M_{13} M_{23} / R_T)}{\partial (x, y, z)} + I_1 \omega^2 \frac{\partial (M_{14} M_{24} / j\omega L_4)}{\partial (x, y, z)} \quad (8)$$

where (x, y, z) represents any point shared by the target and the marker mounted on its surface.

Accordingly, equation (8) represents the response of the receiver to any movement of the *marked target* in the space between the transmitter and the receiver. This response consists of an *imaginary signal* and a *real signal* corresponding to the first and second right-hand-side terms, respectively. As explained before, these two changes represent the *signal error* and the *detection signal*, respectively, (see figure 1).

Experimental realization

1. MITS Tomograph

The MITS system used in the measurements is shown in figures (3-5). It is a modified version of the one described in [10] after redesigning the circular coil system and its whole mechanical structure to an elliptical version approximating the shape of the truncal (thoracic, abdominal and pelvic) parts of the human body.



Fig. 3: The mechanical body and elliptical coil system of the used MITS tomograph. The two-plane transceiver array is fitted in a custom-built, robust wooden table which has some kind of opening mechanism that allows positioning a test person or a large test phantom into the coil system.

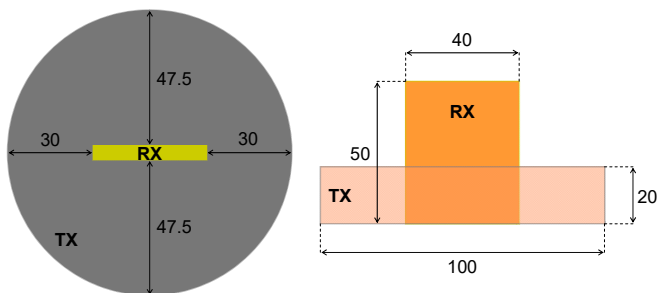


Fig. 4: Geometry of the transmitter (TX) and the receiver (RX) forming the transceiver. Left: front view, right: top view. All dimensions are given in [mm].

The coil system has a two-plane elliptical array of transceivers (TRX), an upper and a lower plane with 8 TRXs each. Every TRX consists of an air-core solenoid (16 turns) serving as the transmitter (TX) and a *planar zero flow coil PZFC* (36 turns) etched on a PCB serving as the receiver (RX) [11, 12]. All components were properly shielded in order to

reduce the capacitive coupling between them as well as other external electromagnetic interferences.

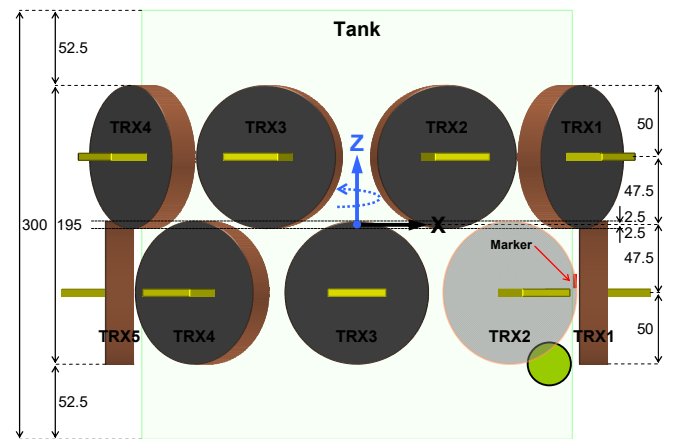
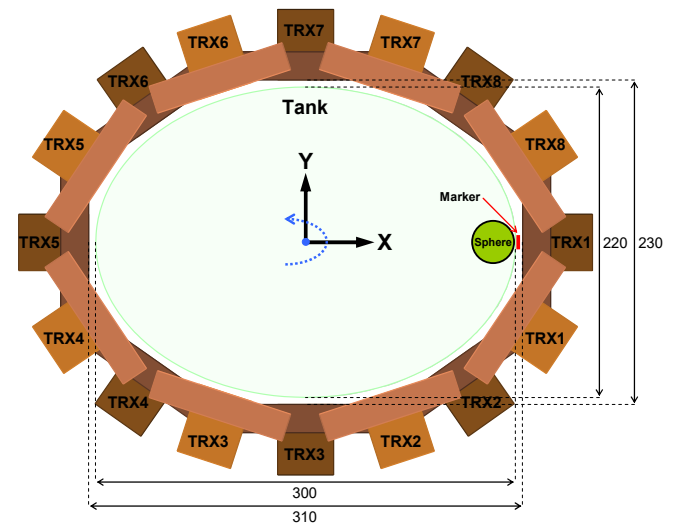


Fig. 5: Experimental setup and geometry of the coil system. Top: top view, bottom: long-side view; TRX: transceiver. For the sake of clarity, the lower TX2 was made transparent and its 3D view was deactivated. The red marker in the figure is either an active or a passive one, depending on the experiment. The dotted, curved blue arrow symbolizes an unwanted (rotational) movement of the measured medium. All dimensions are given in [mm].

2. Measurement setup

The measurement setup is depicted in figure (5). A saline sphere of 15 mm radius and 2 S/m conductivity served as a measurement object representing the region of interest (ROI). It was prepared from a mixture of NaCl solution and agar powder (*VOLLKRAFT*) in the following way:

- NaCl solution of 2 S/m conductivity was heated in a microwave oven and taken out before boiling in order to avoid any NaCl concentration change through vaporization and hence any change in the intended conductivity.
- Afterwards, agar powder was mixed with the NaCl solution and the mixture was heated again and taken

out before the formation of any bubbles or scum in order to avoid any inhomogeneities.

- A spherical plastic mould of 15 mm radius was filled with the mixture and cooled. The mould was pretreated with a very thin layer of a neutral lubricant (petroleum jelly) in order to avoid adhesion of and hence fissures in the sphere when taking it out of the mould after cooling.

In that way, the produced saline sphere got a gelatinous body with a homogeneous conductivity distribution.

The tank containing the sphere, manufactured in form of an elliptical cylinder, served as a conducting background medium filled with NaCl solution of 0.2 S/m conductivity (10% compared to that of the ROI).

The used active marker was a single-turn circular coil with 10 mm diameter. The periodic frame-wise on-off operation of the marker was realized by means of software-controlled switching of an N-channel enhancement mode MOSFET, BSN20 (Philips Semiconductors). Care was taken to avoid the induction of parasitic eddy currents by the marker or its circuit and thereby the contamination of the phantom signal, particularly at high frequencies. In this respect, the MOSFET was chosen to be a tiny plastic-packaged SMD mounted outside the sensitive region of the coil system. Moreover, the copper wire forming the marker loop was as thin as 0.1 mm. The MOSFET-switched marker circuit was implemented in the same way used in [7].

The passive marker was made of soft ferrite, namely, nickel-zinc ferrite powder, K 250 (Kaschke Components). The powder was pressed in the shape of a thin square plate with $L \times W \times H$ of $10 \times 10 \times 0.1$ mm. According to the manufacturer's specification, the K 250 has a complex relative permeability $\{\mu_r = \mu_r' - j * \mu_r'' \approx 200 - j * 1.6\}$ at 1 MHz. This yields a loss factor of about $\{\mu_r''/\mu_r' \approx 0.008\}$, or inversely, a quality factor of about $\{\mu_r'/\mu_r'' \approx 125\}$, and hence an almost negligible loss μ_r'' within the low part of the β -dispersion frequency range. The DC-resistivity of the K 250 is specified to be $\geq 10^5 \Omega \cdot m$ at 25 °C representing the temperature of the measurement environment in the laboratory.

The active and passive markers were fixed on the lateral surface of the tank. The red marker shown in figure (5) represents both kinds of markers; however, the corresponding measurements were performed separately, i.e., the tank was marked with only one of them in two independent experiments.

3. Measurement process

All error detection measurements, whether with an active or a passive marker, were carried out at 200 and 500 kHz simultaneously; at these two frequencies, the TXs were driven by excitation currents of 0.46 and 0.34 A_{rms}, respectively. All measurements were state-differential with

15 signal frames acquired in each state with the passive marker, and with 2x15 signal frames acquired in each state with the active marker corresponding to the on and off phases, respectively.

Each experiment consisted of three phases according to the following states:

1. Unmarked saline tank without the sphere (pure background), oriented with its z-axis along the z-axis of the coil system as shown in figure (5). The resulting signal is called \mathbf{v}_{bg} (background signal)
2. Marked saline tank with the same orientation but with the sphere inserted into the tank at the position (135, 0, -97.5) mm. The resulting signal is called $\mathbf{v}_{err-free}$ (error-free signal).
3. Simulated unintentional movement by rotating the whole phantom (marked saline tank including the sphere) by ca. 4° about the z-axis (corresponding to 1 cm arc length), yielding a new position of the sphere at (134, 9, -97.5) mm. The resulting signal is called \mathbf{v}_{err} (erroneous signal).

Each of the data vectors \mathbf{v}_{bg} , $\mathbf{v}_{err-free}$ and \mathbf{v}_{err} consists of 256 entries corresponding to the 256 independent TX-RX measurement combinations. Each entry was calculated as the mean value of the 15 acquired signal frames in each state.

Subtracting $\mathbf{v}_{err-free}$ from \mathbf{v}_{err} yields a difference $\Delta \mathbf{v}_{error}$ which is split up into real and imaginary parts according to the following two equations, respectively:

$$Im(\Delta \mathbf{v}_{error}) = Im(\mathbf{v}_{err}) - Im(\mathbf{v}_{err-free}) \quad (9)$$

$$Re(\Delta \mathbf{v}_{error}) = Re(\mathbf{v}_{err}) - Re(\mathbf{v}_{err-free}) \quad (10)$$

$Im(\Delta \mathbf{v}_{error})$ represents a signal error which would corrupt image reconstruction, whereas $Re(\Delta \mathbf{v}_{error})$ represents a detection signal to be used to detect the onset of $Im(\mathbf{v}_{err})$, i.e., to detect $Im(\Delta \mathbf{v}_{error})$.

Accordingly, the total received signal consists of both 15-frame signals acquired before and after the simulated unwanted movement, $\mathbf{v}_{err-free}$ and \mathbf{v}_{err} , respectively. This 30-frame signal is corrupted by $\Delta \mathbf{v}_{error}$ and will hence produce erroneous images independent of the applied type of imaging, whether static (absolute), dynamic or parametric (differential). In this study, the erroneous images were reconstructed state-differentially. The corresponding erroneous signals, termed $\Delta \mathbf{v}_{err}$, were obtained through averaging the 30-frame total received signal and subtracting it from \mathbf{v}_{bg} , i.e., with respect to the imaginary part:

$$Im(\Delta \mathbf{v}_{err}) = Im(\mathbf{v}_{bg}) - mean(Im(\mathbf{v}_{err-free}) + Im(\mathbf{v}_{err})) \quad (11)$$

In order to correct $\Delta\mathbf{v}_{err}$ and hence the erroneous images, the signal error $Im(\Delta\mathbf{v}_{error})$ was eliminated in two steps by means of the D&E technique. In a first step, the IoT was extracted from the *detection signal* $Re(\Delta\mathbf{v}_{error})$. In a second step, the erroneous frames \mathbf{v}_{err} were discarded, while the error-free ones $\mathbf{v}_{err-free}$ were retained. $\mathbf{v}_{err-free}$ was then used to reconstruct the corrected (artefact-free) images. The corresponding corrected signals, termed $\Delta\mathbf{v}_{corr}$, were obtained through subtracting $\mathbf{v}_{err-free}$ from \mathbf{v}_{bg} , i.e., with respect to the imaginary part:

$$Im(\Delta\mathbf{v}_{corr}) = Im(\mathbf{v}_{bg}) - Im(\mathbf{v}_{err-free}) \quad (12)$$

In order to assess the reproducibility of the D&E-corrected signals and images, they were compared to reference (true) ones gained from separate measurements without medium rotation and the marker. These *reference measurements* had the same settings mentioned hereinabove and the same setup shown in figure (5) except the marker. The resulting true signals, termed $\Delta\mathbf{v}_{true}$, were used for the reconstruction of the true images, and can be presented as follows with respect to the imaginary part:

$$Im(\Delta\mathbf{v}_{true}) = Im(\mathbf{v}_{bg}) - Im(\mathbf{v}_t) \quad (13)$$

where \mathbf{v}_t and \mathbf{v}_{bg} represent the total and background signals, respectively.

The comparison between the corrected and true signals $Im(\Delta\mathbf{v}_{corr})$ and $Im(\Delta\mathbf{v}_{true})$ was established through quantifying the discrepancy by using the percentage error $\delta_{\%}$ between the two signals:

$$\delta_{\%} = 100\% \frac{Im(\Delta\mathbf{v}_{true}) - Im(\Delta\mathbf{v}_{corr})}{Im(\Delta\mathbf{v}_{true})} \quad (14)$$

where the signals $\Delta\mathbf{v}_{corr}$ and $\Delta\mathbf{v}_{true}$ represent one entry in the data vectors $\Delta\mathbf{v}_{corr}$ and $\Delta\mathbf{v}_{true}$ (taken from equations 12 and 13, respectively) corresponding to the measurement combination TX1-RX1 of the lower TRX plane. This entry was chosen because it has the greatest impact on the corresponding image because the sphere and the marker were located in front of the lower TRX1 (see figure 5).

The signal-to-noise ratio *SNR* was calculated according to the following common formula:

$$SNR = 20 \log \frac{|\Delta\mathbf{v}_{\#}|}{N} \quad (15)$$

where the signal $\Delta\mathbf{v}_{\#}$ represents, again, the entry of the lower TRX1 in the data vectors $\Delta\mathbf{v}_{\#}$ ($\Delta\mathbf{v}_{error}$, $\Delta\mathbf{v}_{err}$, $\Delta\mathbf{v}_{corr}$ or $\Delta\mathbf{v}_{true}$ taken from equations 9-13), and the noise N

represents the standard deviation of $\Delta\mathbf{v}_{\#}$ over the acquired signal frames (no notation $Im(\Delta\mathbf{v}_{\#})$ or $Im(N)$ is used in equation 15 because it was also used for the calculation of the *SNR* of the *detection signals* $Re(\Delta\mathbf{v}_{error})$).

Image reconstruction

The forward and inverse problems are formulated, respectively, as:

$$\mathbf{v} = s(\boldsymbol{\sigma}) \quad (16)$$

$$\boldsymbol{\sigma} = s^{-1}(\mathbf{v}) \quad (17)$$

where s is a nonlinear forward operator which represents the governing physics of the MITS problem and maps the distributed conductivities $\boldsymbol{\sigma}$ in the FEM-discretized target medium onto the induced voltages \mathbf{v} in the receivers (FEM: finite element method).

The nonlinear MITS inverse problem is known to be highly ill-posed and underdetermined. Therefore, it has to be carefully tackled in order to attain a stable inverse solution. For this purpose, the implemented solution strategy in this study comprised three main procedures, namely, linearization, optimization and regularization. Linearization is only valid in case of small changes in $\boldsymbol{\sigma}$ which is already fulfilled by the performed state-differential measurements dealing with small conductivity changes caused by weak perturbations. Optimization was based on the least squares estimator (LS). Regularization was realized using the Tikhonov method. It has been already shown that the first iteration of the time-consuming iterative Gauss-Newton algorithm preserves the most relevant features of the image. Thus, due to its computational appropriateness, a single-iteration Gauss-Newton reconstructor was preferred for the solution.

Correspondingly, an LS-optimized Tikhonov-regularized solution of the linearized MITS inverse problem using a one-step Gauss-Newton formulation was applied in image reconstruction according to the following equation:

$$Im(\Delta\boldsymbol{\sigma}_{\#}) = \mathbf{S}^T (\mathbf{S}\mathbf{S}^T + \lambda \mathbf{I}_m)^{-1} Im(\Delta\mathbf{v}_{\#}) \quad (18)$$

where \mathbf{S} is the sensitivity (Jacobian) matrix representing the rate at which \mathbf{v} changes in response to a change in $\boldsymbol{\sigma}$, i.e., $\{\mathbf{S} = \partial\mathbf{v}/\partial\boldsymbol{\sigma}\}$, and was calculated for the non-rotated tank because \mathbf{S} remained almost unchanged after the slight rotation of 4° ; $\Delta\boldsymbol{\sigma}_{\#}$ ($\Delta\boldsymbol{\sigma}_{err}$, $\Delta\boldsymbol{\sigma}_{corr}$ or $\Delta\boldsymbol{\sigma}_{true}$) is the small change in the conductivity between two different states of the target, and $\Delta\mathbf{v}_{\#}$ ($\Delta\mathbf{v}_{err}$, $\Delta\mathbf{v}_{corr}$ or $\Delta\mathbf{v}_{true}$) is the corresponding change in the measured signal at the receivers which will be taken from equations (11, 12, 13) depending on the kind of images to be reconstructed: erroneous, corrected or true images, respectively; λ and \mathbf{I}_m (identity matrix) are the

regularization parameter and regularization matrix, respectively.

The adequate regularization parameter λ was determined as:

$$\lambda_{app} = \text{mean}\{\text{var}\{Im(\Delta\mathbf{v}_{\#})\}\} \quad (19)$$

where λ_{app} represents an *appropriate regularization parameter*; *mean* and *var* denote the mean value and variance of the bracketed quantity over the acquired signal frames.

Thus, the determination of λ is based on the variances of the acquired data vectors $\Delta\mathbf{v}_{\#}$. Hence, the regularization term (λI_m) in equation (18) is an approximation of the covariance matrix of the data assuming negligible off-diagonal terms and equal variance in all TX-RX channels. This choice fairly meets the requirement that the variance of the residuals and of the data noise approach each other. It has been found that equation (19) yields an appropriate λ if the ratio between the standard deviation of the data variances and the mean of these variances is lower than one order of magnitude, i.e., in mathematical terms:

$$\frac{sd\{\text{var}\{Im(\Delta\mathbf{v}_{\#})\}\}}{\text{mean}\{\text{var}\{Im(\Delta\mathbf{v}_{\#})\}\}} < 10 \quad (20)$$

where *sd* denotes the standard deviation of the bracketed quantity over the acquired signal frames.

In addition, λ_{app} allows avoiding under- or over-regularization of the inverse solution and hence the aimed images, particularly if condition (20) is adequately met.

In this work, there were 10 different images of $Im(\Delta\sigma_{\#})$ to be reconstructed corresponding to the 10 different $Im(\Delta\mathbf{v}_{\#})$:

- $Im(\Delta\mathbf{v}_{err})$ gained from the *error detection measurements* with an active and a passive marker at 200 and 500 kHz yielding 4 images.
- $Im(\Delta\mathbf{v}_{corr})$ for each $Im(\Delta\mathbf{v}_{err})$ yielding another 4 images.
- $Im(\Delta\mathbf{v}_{true})$ gained from the *reference measurements* at 200 and 500 kHz yielding 2 images.

Due to the single-step nature of the used Gauss-Newton image reconstruction algorithm, no absolute conductivity changes can be reconstructed; thus the used colour bars will only serve to qualitatively estimate the contrast between the ROI and the background or between 200 and 500 kHz. However, using the same regularization parameter for all reconstructions allows for better quantitative comparison between the different images $Im(\Delta\sigma_{\#})$ with respect to the different signals $Im(\Delta\mathbf{v}_{\#})$. This choice was possible thanks to the high SNR at 200 kHz (51.29 - 56.91 dB). The global λ_{app} was obtained by applying equation (19) to all 10 data vectors $\Delta\mathbf{v}_{\#}$ at once, i.e., by

averaging over all 10 $\Delta\mathbf{v}_{\#}$. The resulting λ_{app} of 4.23×10^{-17} was found to be an adequate choice for the reconstruction of all images.

In order to introduce additional comparability measures between the different images, their contrast-to-noise ratio *CNR* and the involved quantities were provided. The *CNR* of the image $\Delta\sigma_{\#}$ was defined as:

$$CNR = \frac{Im(\Delta\sigma_{\#})}{Im(N_{bg})} \quad (21)$$

where the entry $\Delta\sigma_{\#}$ was chosen as the central element (centre of gravity) of the reconstructed spherical perturbation (ROI) which was very close to the mean value of the ROI elements, and the image background noise N_{bg} was calculated as the standard deviation of the image background elements surrounding the ROI.

Ethical approval

The conducted research is not related to either human or animal use.

Results and discussion

Figure (6) shows the reconstructed erroneous images with an active and a passive marker at 200 and 500 kHz. The corrected versions thereof according to the D&E approach are shown in figure (8). The reconstructed true images at 200 and 500 kHz are shown in figure (9). All slices are transversal cross sections taken through the centre of the sphere at $z = -97.5 \text{ mm}$. For the sake of clarity and comparability, a zoom-in screenshot of the ROI and the surrounding background is placed to the right of each image. Some relevant performance parameters that quantify the reconstructed images $Im(\Delta\sigma_{\#})$ in figures (6), (8) and (9) and the corresponding signals $Im(\Delta\mathbf{v}_{\#})$ are summarized in tables (1, 2), (5, 6) and (7, 8), pairwise respectively. Each row in each table corresponds to an image in the respective figure.

As can be seen in figure (6), the rotational movement of the target medium resulted in motion blurring of the reconstructed spherical perturbation in its movement direction (see figure 5). The images gained from the *error detection measurements* with an active marker at 200 and 500 kHz closely resemble those ones gained with a passive marker, respectively. This can be seen qualitatively through a visual inspection as well as quantitatively when comparing the respective image performance parameters in table (2). As can be seen in table (1), this close resemblance is logically expected as the images resulted from quasi-equal imaginary signals in the *error detection measurements*, respectively, and the only difference between both measurements was the used marker affecting the real part of the received signal. Moreover, aside from the performance quantification measures in

table (2), the images gained at 200 kHz are visually similar to those at 500 kHz. The difference is merely in the extent of the background ringing, to be discussed later. At a relatively low frequency of 200 kHz, in spite of the low sensitivity in comparison to that at 500 kHz, an imaginary signal of about 2 μV (see table 1) was sufficient to recognize the shift of the spherical perturbation as clearly as at 500 kHz.

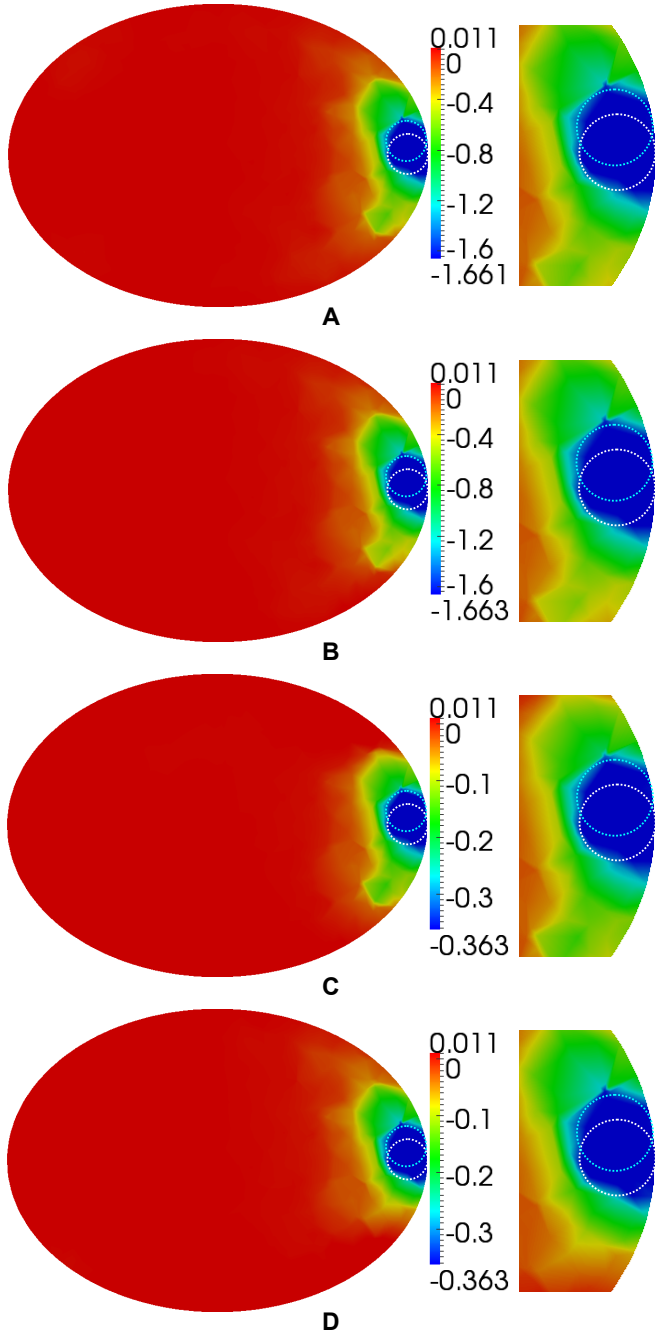


Fig. 6: Reconstructed images $Im(\Delta\sigma_{err})$ of the rotated target medium in the error detection measurements. A: with an active marker at 500 kHz, B: with a passive marker at 500 kHz, C: with an active marker at 200 kHz, D: with a passive marker at 200 kHz. The dotted white and cyan circles mark the initial and final positions of the sphere before and after rotation, respectively.

In order to get rid of the shift artefact affecting the reconstructed sphere in all images of figure (6), the frame-wise behaviour of the imaginary part of the total received signal containing the *signal error* $Im(\Delta v_{error})$ have at first to be inspected together with that of its real part containing the *detection signal* $Re(\Delta v_{error})$ throughout the 30-frame measurement cycle.

The two signals are shown in figure (7), and the quantitative information on $Re(\Delta v_{error})$ and $Im(\Delta v_{error})$ are summarized in tables (3, 4), respectively.

Marker	Image	f [kHz]	$Im(\Delta v_{err})$ [V]	$Im(N)$ [V]	SNR [dB]
Active	A	500	-10.09×10^{-6}	4.94×10^{-9}	66.20
	C	200	-2.27×10^{-6}	5.28×10^{-9}	52.67
Passive	B	500	-10.11×10^{-6}	4.91×10^{-9}	66.27
	D	200	-2.27×10^{-6}	6.19×10^{-9}	51.29

Table 1: Some quantitative data on the erroneous signals $Im(\Delta v_{err})$ relevant to the erroneous images $Im(\Delta\sigma_{err})$ in figure (6).

Marker	Image	f [kHz]	$Im(\Delta\sigma_{err})$ [S/m]	$Im(N_{bg})$ [S/m]	CNR
Active	A	500	-1.661	2.856×10^{-2}	58.16
	C	200	-0.363	0.815×10^{-2}	44.54
Passive	B	500	-1.663	2.824×10^{-2}	58.89
	D	200	-0.363	0.802×10^{-2}	45.26

Table 2: Some quantitative data on the erroneous images $Im(\Delta\sigma_{err})$ in figure (6).

As can be seen in figure (7), independent of the used type of marker or the applied frequency in the error detection measurements, the real signal shows a jump at the 31st frame. This jump indicates the occurrence of a movement during measurement wherefore another jump at the very same frame can be seen in the imaginary signal. Actually, it is not necessarily important in this discussion to recognize the jump in the imaginary signal; of paramount importance is to manifestly recognize the jump in the real signal because this jump represents the wanted *detection signal* $Re(\Delta v_{error})$ and hence the key to pinpointing the corresponding searched-for *signal error* $Im(\Delta v_{error})$ in the imaginary signal. Despite that, the sphere was intentionally chosen to be of a relatively high conductivity of 2 S/m for reasons of clarity and comprehensibility; if a human brain had been measured instead, it would not have been possible to distinguish the *signal error* $Im(\Delta v_{error})$ (imaginary jump) in the green curves of figure (7). Therefore, it is a matter of course that the marker must induce sufficiently strong *detection signals* $Re(\Delta v_{error})$, even in case of pretty slight movements of the order of [mm].

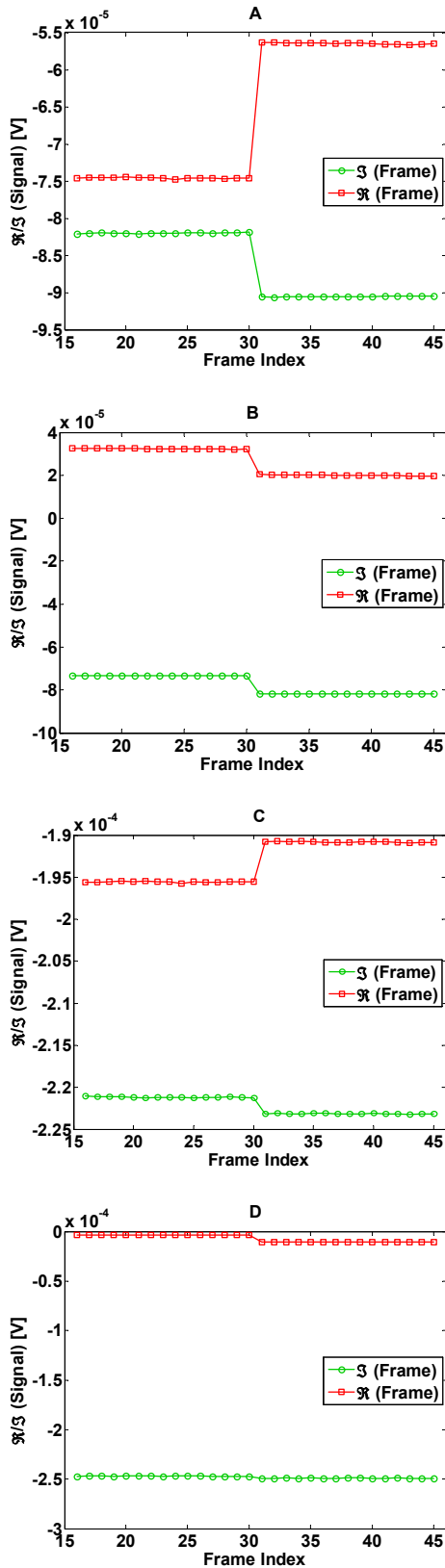


Fig. 7: Acquired real and imaginary frames of the total received signal before and after medium rotation in the *error detection measurements*. A: with an active marker at 500 kHz, B: with a passive marker at 500 kHz, C: with an active marker at 200 kHz, D: with a passive marker at 200 kHz. Green curve: imaginary signal showing the *signal error* $Im(\Delta v_{error})$ to be eliminated; red curve: real signal showing the *detection signal* $Re(\Delta v_{error})$ to be used to detect $Im(\Delta v_{error})$. Note the differently scaled y-axes of the graphs. The first invisible 15 frames (1 - 15) were used for phase calibration purposes [13] and are therefore not shown.

Marker	Graph	f [kHz]	$Re(\Delta v_{error})$ [V]	$Re(N)$ [V]	SNR [dB]
Active	A	500	18.18×10^{-6}	4.42×10^{-9}	72.28
	C	200	4.75×10^{-6}	5.90×10^{-9}	58.12
Passive	B	500	-12.38×10^{-6}	6.20×10^{-9}	66.01
	D	200	-7.15×10^{-6}	4.71×10^{-9}	63.63

Table 3: Some quantitative data on the *detection signals* $Re(\Delta v_{error})$ in figure (7).

Marker	Image	f [kHz]	$Im(\Delta v_{error})$ [V]	$Im(N)$ [V]	SNR [dB]
Active	A	500	-8.56×10^{-6}	3.75×10^{-9}	67.17
	C	200	-1.96×10^{-6}	5.01×10^{-9}	51.85
Passive	B	500	-8.55×10^{-6}	3.58×10^{-9}	67.56
	D	200	-1.96×10^{-6}	5.33×10^{-9}	51.31

Table 4: Some quantitative data on the *signal errors* $Im(\Delta v_{error})$ in figure (7).

In spite of that, the small dimensions of the used markers (active: 1 cm diameter, passive: $1 \times 1 \times 0.1$ cm = $L \times W \times H$) were intentionally chosen insomuch that they produce *detection signals* $Re(\Delta v_{error})$ about of the order of the *error signals* $Im(\Delta v_{error})$ at the applied frequencies (see tables 3, 4). Thus, both presented kinds of markers, even though small, induced indeed adequate detection signals and are due to their small dimensions very convenient for real applications.

According to the D&E mechanism, the abovementioned 31st frame, at which the sudden signal change in figure (7) occurred due to target movement, marks the required IoT for the removal of the erroneous data which produced the blurred images in figure (6), i.e., $IoT = 31$. Thus, all imaginary frames with index $i \geq 31$ were discarded, whereas those useful ones with index $i < 31$ (except the calibration frames, i.e., $15 < i < 31$) were used for movement-artefact-free imaging as shown in all images of figure (8) obtained after applying the D&E method.

As can be seen in figure (8), there is a close similarity between the corrected images at 200 and 500 kHz, respectively. Again, on the one hand, this close similarity can be predicted when comparing the respective imaginary signals in table (5); on the other hand, it is qualitatively as well as quantitatively evident when comparing the respective performance indicators in table (6). Moreover, the images are visually similar independent of the applied frequency. Being similar, however, is not of that relevance to the discussion; of most relevance are actually the consequences of the applied D&E technique on the movement artefacts apparent in all target images in the previous figure (6). Comparing now the erroneous images in figure (6) with their corrected versions in figure (8), it can be clearly seen that the motion artefacts, i. e., the considerable blurring, have disappeared (compare the zoom-in screenshots of both groups of images). The

remaining slight blurring of the reconstructed sphere in figure (8) is thus not any more a consequence of motion, but only due to the broad main lobe of the point spread function (PSF) being typical of MITS, including also the characteristic ringing artefacts which are caused by the oscillating and attenuating side lobes of the PSF. This can be attributed to the non-edge-preserving properties of the used Tikhonov regularization method.

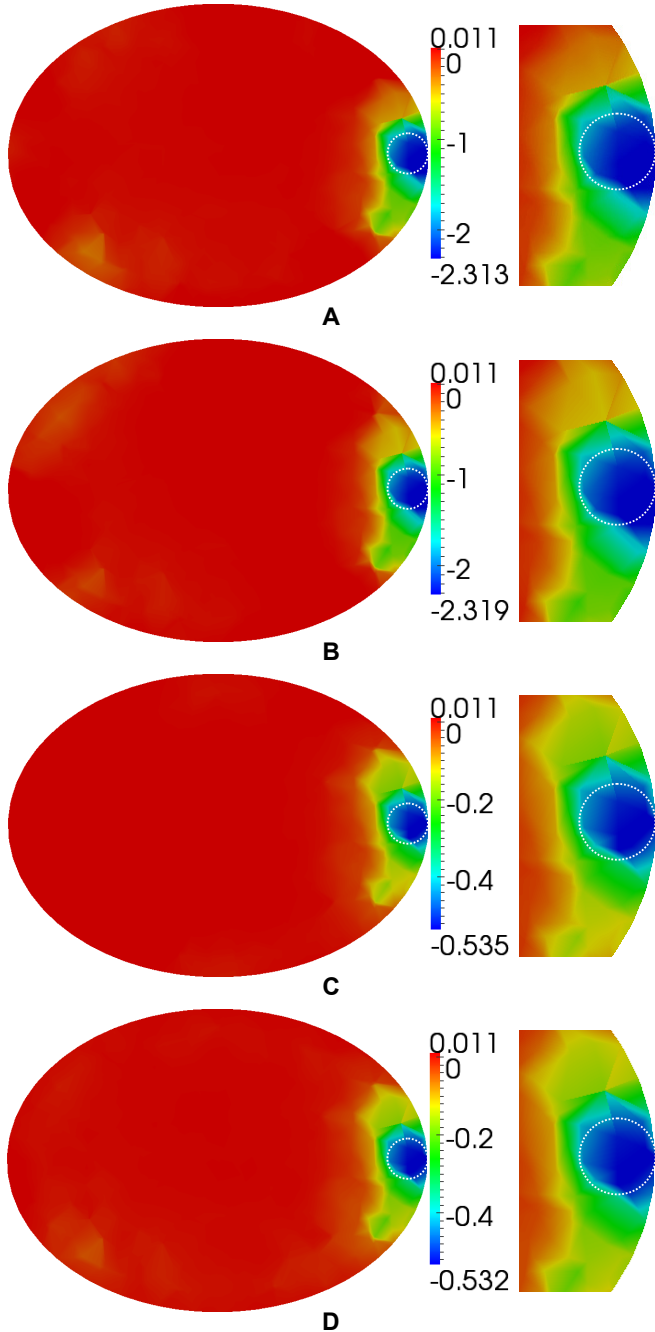


Fig. 8: Corrected versions $Im(\Delta\sigma_{corr})$ of the erroneous images $Im(\Delta\sigma_{err})$ in figure (6), respectively, after applying the D&E technique. The dotted white circle marks the same initial position of the sphere before rotation in the error detection measurements.

Image	f [kHz]	$Im(\Delta v_{corr})$ [V]	$Im(N)$ [V]	SNR [dB]
A	500	-14.11×10^{-6}	6.15×10^{-9}	67.21
C	200	-3.34×10^{-6}	5.55×10^{-9}	55.59
B	500	-14.15×10^{-6}	6.21×10^{-9}	67.15
D	200	-3.32×10^{-6}	7.06×10^{-9}	53.45

Table 5: Some quantitative data on the corrected signals $Im(\Delta v_{corr})$ relevant to the corrected images $Im(\Delta\sigma_{corr})$ in figure (8).

Image	f [kHz]	$Im(\Delta\sigma_{corr})$ [S/m]	$Im(N_{bg})$ [S/m]	CNR
A	500	-2.313	4.351×10^{-2}	53.16
C	200	-0.535	1.183×10^{-2}	45.22
B	500	-2.319	4.289×10^{-2}	54.07
D	200	-0.532	1.233×10^{-2}	43.15

Table 6: Some quantitative data on the corrected images $Im(\Delta\sigma_{corr})$ in figure (8).

Thus, the movement artefacts could be successfully eliminated by means of the D&E technique. In order to ascertain this statement even more and to demonstrate the good reproducibility of the measurements, the D&E-corrected images in figure (8) were compared to the true ones of the non-rotated target in figure (9).

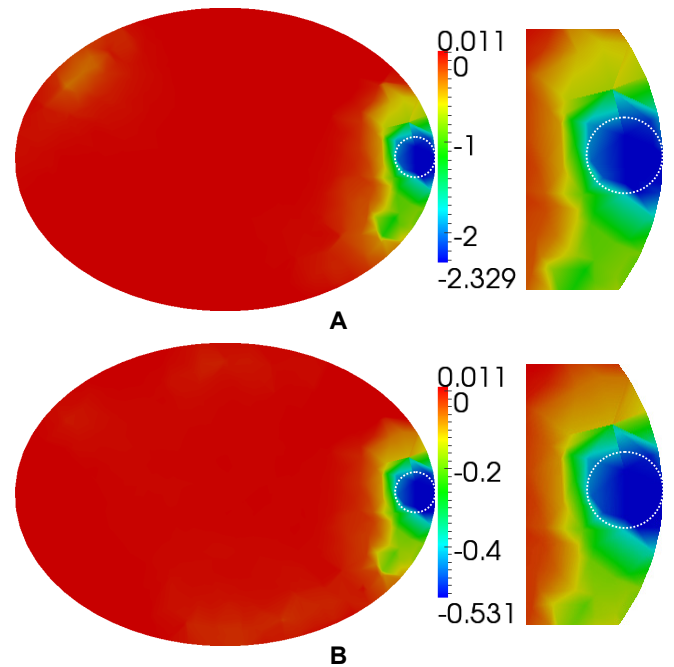


Fig. 9: Reconstructed images $Im(\Delta\sigma_{true})$ of the non-rotated target medium in the reference measurements. The dotted white circle marks the position of the sphere which was identical to the initial position of the sphere before rotation in the error detection measurements.

Image	f [kHz]	Im(Δv_{true}) [V]	Im(N) [V]	SNR [dB]
A	500	-14.21×10^{-6}	6.65×10^{-9}	66.60
B	200	-3.30×10^{-6}	4.71×10^{-9}	56.91

Table 7: Some quantitative data on the true signals $Im(\Delta v_{true})$ relevant to the true images $Im(\Delta \sigma_{true})$ in figure (9).

Image	f [kHz]	Im($\Delta \sigma_{true}$) [S/m]	Im(N_{bg}) [S/m]	CNR
A	500	-2.329	4.327×10^{-2}	53.82
B	200	-0.531	1.205×10^{-2}	44.07

Table 8: Some quantitative data on the true images $Im(\Delta \sigma_{true})$ in figure (9).

As can already be expected from tables (5, 7), the corrected images in figure (8) and the corresponding cumulative data in table (6) deviate only negligibly from the true ones in figure (9) and table (8), respectively. Table (9) summarizes the percentage error $\delta\%$ and therewith the good agreement between the corrected and true signals.

f [kHz]	Im(Δv_{true}) [V]	Im(Δv_{corr}) [V]	$\delta\%$
500	-14.21×10^{-6}	-14.11×10^{-6}	0.70
		-14.15×10^{-6}	0.42
200	-3.30×10^{-6}	-3.34×10^{-6}	1.21
		-3.32×10^{-6}	0.61

Table 9: Accuracy of the corrected signals $Im(\Delta v_{corr})$ with respect to the true signals $Im(\Delta v_{true})$. $Im(\Delta v_{corr})$ and $Im(\Delta v_{true})$ are taken from tables (5, 7), respectively, where in case of $Im(\Delta v_{corr})$ there are two values per frequency because the original error detection measurements were conducted with an active and a passive marker at each frequency.

The small average percentage error of less than 1% has most probably been caused by noise and some possible additional experimental (human) error, e.g., 1 mm positioning inaccuracy of the sphere inside the tank on the x-, y- or z-axis.

The contactless measurement manner of MITS is considered as a key advantage of this imaging modality because many other advantages are related thereto. In contrast to active D&E, this advantage remains unaffected in case of passive D&E as there is no need for any additional electronics and related accessories whatsoever to be mounted on or connected to the patient. In this respect, if it is of interest to keep the MITS measurement contactless in case of active D&E, the loop can be simply permanently short-circuited during measurement. Thus, the active marker becomes a passive marker, and the on-off switching and the related technical implementation are no more required. This proposal was successfully tried using the same previous single-loop marker short-circuited in D&E experiments conducted in the same way described

previously. The results were expectedly very similar to those of active D&E with the MOSFET-switched coil marker shown in this study.

The use of active markers is beneficial for distinguishing the marker signal from other unwanted changes in the real part of the MITS signal, e.g., transmitter and/or receiver displacements, etc., because the modulation by the periodic on-off cycling yields a specific signature of the marker. In case of D&E with passive coil markers, this distinction is not possible; however, on the other side, its advantages are the simple and costless implementation as well as the contact-free and shorter measurements; therefore, its use may pay off in many practical situations. Anyway, of most relevance in this regard is the produced detection signal itself; as shown in graph (C) of figure (7) and in the corresponding row of table (3), a detection signal as low as $4.75 \mu V$ was sufficient to successfully accomplish the error detection procedure of the D&E process, i.e., to exactly identify the aimed IoT.

Conclusion

The obtained qualitative and quantitative measurement and image reconstruction results in the physiological conductivity range and β -dispersion frequency range support the applicability of the novel D&E technique in measurement optimization in biomedical MITS. Elimination of misleading movement artefacts in biomedical MITS images represents an important advancement of such an imaging modality being already known for its low-spatial resolution. The practicality of the suggested D&E methodology through offering two different types of markers for target motion detection facilitates the associated measurement process. Advantage can be taken of each type depending on the available measurement setup and the underlying application. While passive D&E is almost costless, very simple to implement, does not prolong the acquisition time and retains the MITS measurement contactless, active D&E offers a parallel measurement of an unmarked target and therewith the choice between two versions of the biological signal as well as the characteristic signature mentioned hereinbefore. Moreover, the non-permanent active marker can be shorted during measurement and hence used as a permanent passive marker. Additionally, it has been shown that markers, whether active or passive ones, of large dimensions ought not necessarily to be used as long as small ones deliver adequate detection signals.

One of the key advantages of the D&E technique is that the required detection information on target motion is gained from the MITS measurement itself; in other words, the detection signal is a part of the total received MITS signal. Thus, there is no need for inconvenient fixation of the patient or installation of additional costly or complex tracking and surveillance devices. As for instance, using a

high-resolution multiple-camera system and/or an array of movement and distance sensors would be expensive and less favourable for the measurement setup on the one hand; on the other hand, such equipments may only provide information about whether unwanted movements occurred or not, but not about the exact frames whereat these movements possibly occurred unless these equipments are precisely synchronized in some proper way with the multiframe measurement cycle to accomplish this task.

Intuitively, it can be inferred that the same D&E results presented in this study would have been obtained *if the coil system itself rather than the target medium had been rotated in the reverse direction the same angle of 4° about the z-axis, i.e., clockwise* (see figure 5). Accordingly, the proposed D&E technique is as much applicable to the patient as to the coil system; in other words, it can be used for the detection and elimination of signal errors caused by unwanted movements of the patient as well as of the transmitters and/or the receivers. Although important, this issue was beyond the scope of our research because we suppose that coil systems and their supporting mechanics must be well fixed in place in order to avoid any such movements on the one hand, and to provide the image reconstruction algorithm with the exact positions of the transmitters and receivers being one of its most important inputs on the other hand. For these reasons, the used coil system and its mechanical body shown in figure (3) were firmly and robustly constructed.

Finally, it can be stated that the presented D&E technique represents a novel measurement optimization technique in biomedical MITS as there is no need to repeat the time-consuming measuring and imaging processes (except for $IoT = 1$) in case of any movement errors whatsoever. This issue is as much relevant to the examiner as to the patient.

Conflict of interest

Authors state no conflict of interest.

References

1. Korzhenevskii AV, Cherepenin VA. Magnetic induction tomography. J Commun Technol Electron. 1997; 42(4): 469-74.
2. Griffiths H, Stewart WR, Gough W. Magnetic induction tomography: a measuring system for biological tissues. Ann NY Acad Sci. 1999; 873(1): 335-45. <https://doi.org/10.1111/j.1749-6632.1999.tb09481.x>
3. Korjnevsky A, Cherepenin V, Sapetsky S. Magnetic induction tomography: experimental realisation. Physiol Meas. 2000; 21(1): 89-94. <https://doi.org/10.1088/0967-3334/21/1/311>
4. Scharfetter H, Lackner HK, Rosell J. Magnetic induction tomography: hardware for multi-frequency measurements in biological tissues. Physiol Meas. 2001; 22(1): 131-46. <https://doi.org/10.1088/0967-3334/22/1/317>
5. Scharfetter H, Casa-as R, Rosell J. Biological tissue characterization by magnetic induction spectroscopy (MIS): requirements and limitations. IEEE Trans Biomed Eng. 2003; 50(7): 870-80. <https://doi.org/10.1109/TBME.2003.813533>
6. Lanfermann G, Thijs JAJ, Pinter R, Igney CH. Method and apparatus for inductively measuring the bio-impedance of a users body. Patent Application Publication: US 2008/0194982 A1; Aug. 14, 2008.
7. Scharfetter H, Issa S, Gürsoy D. Tracking of object movements for artefact suppression in magnetic induction tomography (MIT). J Phys: Conf Ser. 2010; 224(1): 012040. <https://doi.org/10.1088/1742-6596/224/1/012040>
8. Griffiths H. Magnetic induction tomography. Meas Sci Technol. 2001; 12(8): 1126-31. <https://doi.org/10.1088/0957-0233/12/8/319>
9. Griffiths H. Magnetic induction tomography. In: Holder DS editor. Electrical Impedance Tomography: Methods, History and Applications (Series in Medical Physics and Biomedical Engineering). IOP Publishing: Bristol and Philadelphia. 2005; pp. 213-38.
10. Scharfetter H, Köstinger A, Issa S. Hardware for quasi-single-shot multifrequency magnetic induction tomography (MIT): the Graz Mk2 system. Physiol Meas. 2008; 29(6): 431-43. <https://doi.org/10.1088/0967-3334/29/6/S36>
11. Watson S, Morris A, Williams RJ, Griffiths H, Gough W. A primary field compensation scheme for planar array magnetic induction tomography. Physiol Meas. 2004; 25(5): 271-9. <https://doi.org/10.1088/0967-3334/25/1/031>
12. Scharfetter H, Merwa R, Pilz K. A new type of gradiometer for the receiving circuit of magnetic induction tomography (MIT). Physiol Meas. 2005; 26(2): 307-18. <https://doi.org/10.1088/0967-3334/26/2/028>
13. Scharfetter H, Issa S. Reduction of low-frequency noise in magnetic induction tomography systems. IFMBE Proc. 2008; 22: 752-755. https://doi.org/10.1007/978-3-540-89208-3_180